Available online at www.sciencedirect.com
ScienceDirect
Trans. Nonferrous Met. Soc. China 35(2025) 2734−2746
Transactions of Nonferrous Metals Society of China
www.tnmsc.cn

Wide-azimuth CSEM detection utilizing horizontal and total magnetic field intensities

Di-quan LI[1,2,3], Yun-qi ZHU[1,2,3], Wei-tian WU[1,2,3], Yan-fang HU[1,2,3], Tie-gang TONG[1,2,3]

1. Key Laboratory of Metallogenic Prediction of Nonferrous Metals and Geological Environment Monitoring (Central South University), Ministry of Education, Changsha 410083, China;
2. Hunan Provincial Key Laboratory of Nonferrous and Geological Hazard Detection, Changsha 410083, China;
3. School of Geosciences and Info-physics, Central South University, Changsha 410083, China

Received 26 December 2023; accepted 27 August 2024

Abstract: Traditional controlled source electromagnetic methods (CSEM) typically collect specific single-component of the total magnetic field intensity, leading to zero-value bands, narrow azimuthal detection ranges, and angular detections. An innovative detection strategy that utilized both the horizontal and total magnetic field intensities was introduced in this work. Numerical simulations were conducted to analyze the impact of sensor angular deviations on single-component and horizontal magnetic field intensities. Notably, the horizontal magnetic field intensity remains unaffected by horizontal angle deviations, while the total magnetic field shows resilience to all angular deviations. Theoretically, orthogonal magnetic sensors could facilitate wide-azimuth magnetic field detection. Results from field experiments revealed a pronounced anomaly response of both the horizontal and total magnetic field intensities to underground caverns. These experiments demonstrated a significant reduction in issues related to angular deviations in magnetic sensors and confirmed the feasibility of wide-azimuth magnetic field detection. The proposed wide-azimuth detection method has the potential to extend the detectable angle from that of CSEM to 360°, resolves the issue of angular deviation of magnetic sensors, and thus improves the detection accuracy.

Key words: controlled source electromagnetic method; wide-azimuth; magnetic field; zero-value band; angular deviation

1 Introduction

Frequency-domain controlled source electromagnetic methods (CSEM) conventionally utilize the components of electric and magnetic field intensities to compute apparent resistivity. These methods, including controlled source audio electromagnetic (CSAMT) and wide field electromagnetic method (WFEM), are extensively employed in the mineral exploration and the urban underground surveys [1−5]. However, the measurement of electric field intensity on the ground can present practical challenges. Specifically, the use of copper and unpolarized electrodes requires optimal grounding, a condition that is not always achievable. This can significantly hinder both research progress and the accuracy of detection outcomes [6,7]. Semi-airborne electromagnetic methods (SAEM), transmitting signals from the ground and receiving them via airborne mechanisms, address this challenge by focusing on specific components of the total magnetic field intensities to determine apparent resistivity [8−10]. Despite the magnetic field's lower resolution and shallower detection range compared to the electric field intensity, its ease of deployment and enhanced detection efficiency have expanded its application in

Corresponding author: Yun-qi ZHU, Tel: +86-15675804575, E-mail: yunqizhu@csu.edu.cn
https://doi.org/10.1016/S1003-6326(25)66844-0

resource and subsurface exploration [11−15]. NABIGHIAN [16] introduced the concept of Semi-airborne transient electromagnetic methods (SATEM) and pioneered their use in Australia. This was followed by Canada's development of the first time-domain semi-airborne electromagnetic system, the TerraAir system. Later, the grounded electrical-source airborne transient electromagnetic (GREATEM) system, an SAEM approach with an electrical source, was developed by MOGI et al [17] and tested in Japan, showcasing significant signal enhancement and a superior signal-to-noise ratio. While China initiated research on SAEM systems later than others, efforts spearheaded by key institutions such as the Chinese Academy of Sciences, Jilin University, Chang'an University, and Chengdu University of Science and Technology have been concentrated on the time-domain SATEM [18,19]. Research into the frequency-domain remains comparatively scarce [9,20]. The time-domain approach is particularly effective for near-surface investigations offering robust signals with limited penetration. Conversely, the frequency-domain is more advantageous for probing deeper subsurface regions, owing to its ability to detect weaker signals over an extended range [21,22].

Frequency-domain magnetic field detection within CSEM surveys, whether ground-based or semi-airborne, primarily focuses on individual components such as H_X, H_Y, and H_Z [23−25]. Deploying sources in complex geological terrains presents significant challenges, as each component exhibits zero-value bands that constrain both logistical deployment and the extent of measurable data. The precise orientation of sensors is critical for accurate H_Z acquisition, requiring a horizontal positioning, while H_Y and H_X acquisitions necessitate precise azimuth angle adjustments. In the field, particularly when employing unmanned aerial vehicles (UAVs), achieving this precision becomes problematic due to influences from flight dynamics and wind, which induce sensor orientation errors and result in angular deviations [26−28]. Such deviations can degrade data quality and substantially diminish the effectiveness of the survey.

Historically, research has focused primarily on measurements of single-component of the total magnetic field intensity at static angles, with limited consideration given to the horizontal or total magnetic field intensity analyses. In this work, we introduced a methodology that employs orthogonal coiled magnetic sensors to measure both the horizontal and total magnetic field intensities, effectively addressing the inherent limitations of zero-value bands and angular deviations associated with single-component detections. The findings of this study have significant potential applications in the detection of metal ore resources and underground engineering in areas characterized by complex terrain and mineralization backgrounds.

2 Limitations of single-component magnetic field intensity observations

The magnetic field produced by a horizontal current source on the surface of a homogeneous half-space within a cylindrical coordinate system has an exact expression [29,30]. The radial magnetic field intensity component (H_r) can be represented by the following formula:

$$H_r = -\frac{I\mathrm{d}L}{4\pi r^2}\cdot\left[6I_1K_1 + \mathrm{i}kr(I_1K_0 - I_0K_1)\right]\sin\varphi \quad (1)$$

The tangential magnetic field intensity component (H_φ) is as follows:

$$H_\varphi = \frac{I\mathrm{d}L}{4\pi r^2} I_1K_1\cos\varphi \quad (2)$$

The vertical magnetic field intensity component (H_Z) is as follows:

$$H_Z = -\frac{3I\mathrm{d}L}{2\pi r^4k^2}\cdot\left[1 - \mathrm{e}^{-\mathrm{i}kr}(1 - \mathrm{i}kr - \frac{1}{3}k^2r^2)\right]\sin\varphi \quad (3)$$

In traditional analyses, the magnetic field intensity components along the X- and Y-axes in a Cartesian coordinate system are determined according to Ref. [30]. The magnetic field intensity component along the X-axis (H_X) can be represented by the following formula:

$$H_X = -\frac{I\mathrm{d}L}{4\pi r^2}\cdot\left[8I_1K_1 - \mathrm{i}kr(I_0K_1 - I_1K_0)\right]\sin\varphi\cdot\cos\varphi \quad (4)$$

The magnetic field intensity component along Y-axis (H_Y) is as follows:

$$H_Y = \frac{I\mathrm{d}L}{2\pi r}\left[(1 - 4I_1K_1\cdot\sin^2\varphi + \frac{\mathrm{i}kr}{2}\cdot(I_0K_1 - I_1K_0)\sin^2\varphi\right] \quad (5)$$

where I is the current; I_0 and I_1 are the zero- and first-order Bessel functions of the first kind, respectively; K_0 and K_1 are the zero- and first-order Bessel functions of the second kind, respectively. dL is the polar distance of the source; r is the transceiver distance; φ is the transceiver angle subtended by the midpoint of the source and the observation station; i is the imaginary unit; k is the wavenumber defined by $k^2=-\mathrm{i}\omega\mu\sigma+\omega^2\mu\varepsilon$ (ω is the circular frequency, μ is the magnetic permeability, and σ is the electrical conductivity (inverse of resistivity), and ε is the permittivity). It is established that the total magnetic field intensity at any given point in space remains invariant. Therefore, the sum of the two orthogonal horizontal components, H_r and H_φ, within the cylindrical coordinates, and the corresponding components, H_X and H_Y, in Cartesian coordinates are equivalent, representing the horizontal projections of the total magnetic field intensity. These components can be interconverted utilizing principles of projective transformation.

2.1 Influence of zero-value band

Radiation patterns for the magnetic field intensity components H_X, H_Y, and H_Z are derived through the computational analysis. The model employs a homogeneous half-space with an electrical resistivity of 100 Ω·m and an excitation frequency of 100 Hz. The source is oriented along the X-axis, with its midpoint situated at the coordinate origin, and the polar moment is set at 1 A·m. As Fig. 1 illustrates, H_X and H_Y display four centrosymmetric zero-value zones, while H_Z exhibits two such zones. In conventional electromagnetic surveys, the range within which the field intensity reduces to half its maximum amplitude, considering the signal-to-noise ratio, is typically considered the optimal observation window. The presence of zero-value bands predominantly influences this observational breadth. H_X offers observable ranges of 15°−75° and 105°−165°, H_Y offers an observable range of 55°−125°, and H_Z offers an observable range of 30°−150° [31]. The deployment of sources constitutes a significant portion of the total economic expenditure in CSEM investigations. The suboptimal utilization of sources, due to zero-value restrictions within the single-component observational framework, poses a challenge to large-scale deployment.

2.2 Influence of angle deviation

Achieving precise sensor alignment in field conditions presents significant challenges for single-component measurements. Current ground measurement orientation methods exhibit low accuracy. Furthermore, semi-airborne orientation methods are not only scarce but also less accurate. Figure 2(a) shows the patterns of single-component magnetic field intensity measurements using a hollow coil magnetic sensor. The transceiver angle (φ) defines the detectable range in angle. The component measured by the hollow coil is perpendicular to the coil plane, and the angle with the X-axis can be termed the component angle (θ). When θ=90°, the component is H_Y; when θ=0°, the component is H_X; when the hollow coil plane is horizontal, the component is H_Z. Specifically, when $\theta=\varphi$, the component is H_r, and when $\theta=\varphi$+90°, the component is H_φ. Figure 2(b) shows the schematic diagram of measuring H_Y. The blue solid lines represent the boundary of the detectable angle range bounded by the zero-value bands, and the blue dashed line indicates the detectable distance range, termed the far region. Figures 2(c) and (d) illustrate angular deviation as an example of measuring H_Y. The horizontal rotation of the hollow coil during the measurement of H_Y leads to a decrease in the magnetic field intensity in the Y-direction and an

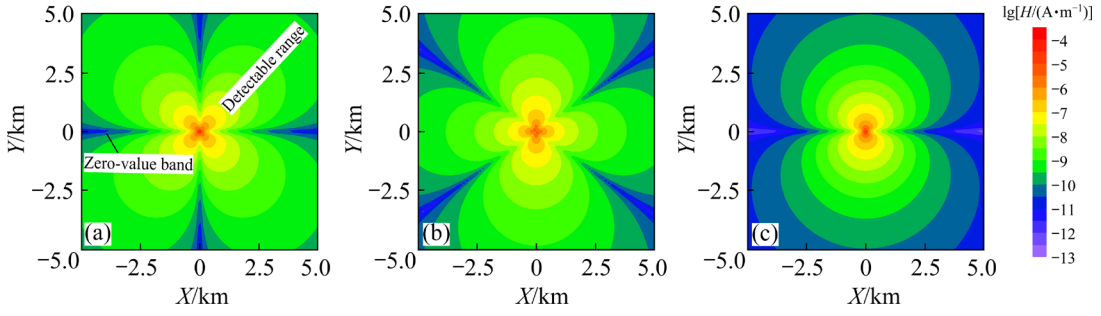

Fig. 1 Radiation patterns of magnetic field intensity components H_X (a), H_Y (b), and H_Z (c) at 100 Hz

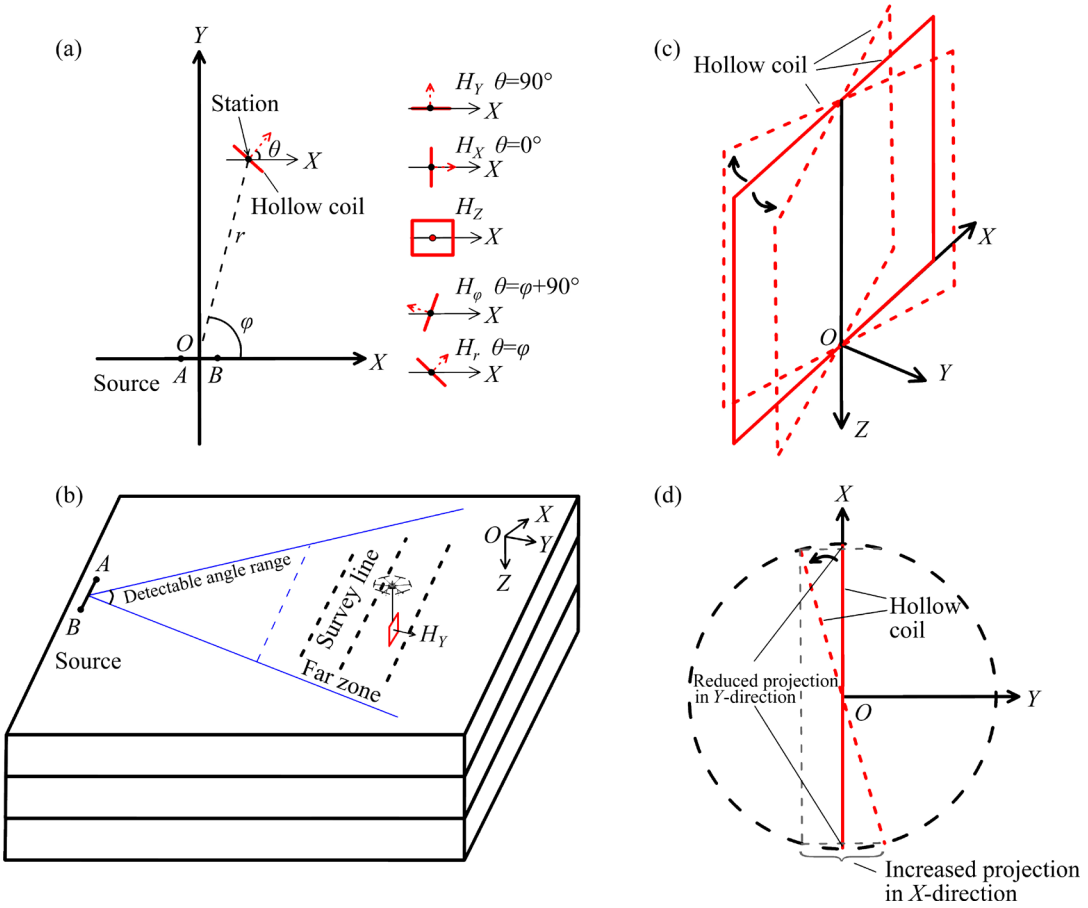

Fig. 2 Top view of single-component magnetic field intensity measurements with hollow coil (a), schematic diagram of measuring H_Y (b), coil deflection (c), and top view of coil deflection (d)

increase in the X-direction, which results in measurement error.

Forward simulation provides a more intuitive visualization of the effects of sensor angular deviations. The computational model employs a uniform half-space with a resistivity of 100 Ω·m. The source is aligned along the X-direction, with its origin at the coordinate center. The polar moment of the source is set at 1 A·m, the transceiver angle is 80°, and the transceiver distance is 10 km. Before discussing the simulation results, it is essential to clarify the parameters, including the induction number (p) (Eq. (6)) and the skin depth (δ) (Eq. (7)) as follows [32]:

$$p=r/\delta \tag{6}$$

$$\delta=356\sqrt{\rho/f} \tag{7}$$

where ρ is the formation resistivity, and f is the frequency. The inductance number p signifies the detectable area in distance, a concept different from the detectable angular range and crucial in frequency-domain electromagnetic methods. The detectable range in distance is a complex parameter related to transceiver distance, formation resistivity, and frequency. Typically, frequency-domain electromagnetic methods operate in the far region where $p \geq 10$. When the observation system is fixed, indicating that both the transceiver distance and the formation resistivity remain constant, p will represent the change in frequency. δ represents the effective penetration depth of an electromagnetic wave and can be utilized to analyze the detection depth.

In Figs. 3(a, d), the variation of H_X is depicted following a 1° deflection of the sensor in both horizontal and vertical directions. The variation of H_X after horizontal deflection is approximately 6.48%, while after vertical deflection, it increases as the induction number decrease, reaching a maximum of 4.00%. Figures 3(b, e) illustrate the changes in H_Y after a 1° deflection of the sensor in

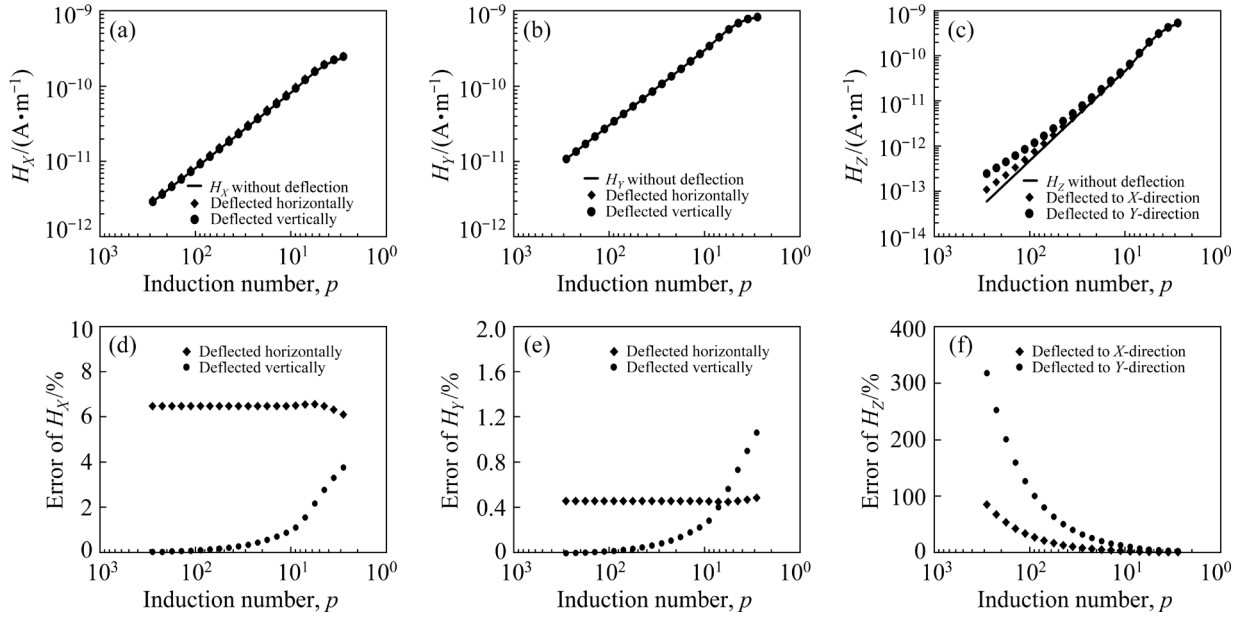

Fig. 3 Variation of H_X (a, d), H_Y (b, e), and H_Z (c, f) following 1° deflection of sensor

both horizontal and vertical directions, specifically for the measurement of H_Y. The amplitude of change after horizontal deflection is small relative to the induction number, while the amplitude of change after vertical deflection increases with the decrease of the induction number but does not exceed 1.50%. Figures 3(c, f) display the changes in H_Z measurement following a 1° deflection of the sensor in both the X- and Y-directions. It is observed that the error after deflection is primarily prominent at higher induction numbers. The error diminishes as the induction number decreases, with a maximum error of 85.14% after deflection in the X-direction, and a maximum error of 316.95% after deflection in the Y-direction.

Each component represents the projected fraction of the total magnetic field intensity in its respective direction, resulting in numeric variations. Specifically, H_Y diminishes with the increase of the transceiver distance, H_X follows a square decay with the increase of the square of the transceiver distance, and H_Z undergoes a fourth-power decay with the increase of the transceiver distance. In the far zone where $p\geq10$, H_Y demonstrates significantly lower angular dependence than H_X and H_Z, with H_Z being the most orientation-sensitive component [24].

In practical detection, sensors may experience deflection in both horizontal and vertical directions. Consequently, the error in acquiring H_Y primarily stems from the loss of the component itself, whereas the errors in acquiring H_X and H_Z predominantly arise from the introduced Y-direction component. Previous studies [11] indicated that the magnetic field intensity at low altitudes closely resembles that on the surface when the ratio of flight altitude to transceiver distance is significantly less than 1. Therefore, issues such as zero-value bands and sensor angular bias arise in single-component magnetic field intensity observations at both ground level and low altitude. It is conceivable that a sensor deflection of 1° could lead to these errors, complicating the accurate estimation and elimination of measurement errors in practical field detection situations, particularly during continuous airborne observations.

3 Feasibility of wide-azimuth detection of horizontal and total magnetic field intensities

The horizontal magnetic field intensity (H_{XOY}) and the total magnetic field intensity (H_{XYZ}) can be derived through component synthesis. For instance, by vectorially combining the orthogonal components H_r and H_φ (or H_X and H_Y), one can yield H_{XOY}:

$$H_{XOY}=(H_r^2+H_\varphi^2)^{1/2}=\frac{I\mathrm{d}L}{4\pi r^2}(R_r^2+R_\varphi^2)^{1/2} \tag{8}$$

where $R_r=[6I_1K_1+\mathrm{i}kr(I_1K_0-I_0K_1)]\sin\varphi$; $R_\varphi=I_1K_1\cos\varphi$.

Similarly, H_{XYZ} results from the vector synthesis of H_r, H_φ, and H_Z (or H_X and H_Y). In practical detection scenarios, two orthogonal horizontal components can be simultaneously gathered and vectorially combined to determine H_{XOY}. Alternatively, three orthogonal components can be collected for the synthesis of H_{XYZ}.

Radiation patterns for H_{XOY} and H_{XYZ} are generated through forward simulation, employing parameters identical to those used in the single-component simulation described in Section 2.1. The model utilizes a homogeneous half-space with an electrical resistivity of 100 Ω·m and an excitation frequency of 100 Hz. The source is aligned along the X-axis with its midpoint positioned at the coordinate origin, and the polar moment is set at 1 A·m. Figure 4 shows that both H_{XOY} and H_{XYZ} exhibit an elliptical shape with the Y-axis as the major axis, and are devoid of zero-value bands. Moreover, these two magnetic field intensities are slightly elevated in the Y-direction, perpendicular to the source. This radiation pattern of the field strength values facilitates the observation of H_{XOY} and H_{XYZ} across all directions within the 0°−360° range, offering a considerable advantage over the single-component magnetic field.

3.1 Effect of angular deviation on horizontal and total magnetic field intensities

According to the vector decomposition and synthesis theory, the total magnetic field intensity, composed of three orthogonal components, is theoretically error-free when subjected to angular deviation. This is because all components of a three-component sensor will be angularly deviated simultaneously, ensuring that the observed components remain orthogonal, thus not affecting the synthetic H_{XYZ}. When using orthogonal two-component sensors to collect H_{XOY}, no error occurs with angular deviation in the horizontal direction. However, an error still arises with vertical deviation. Simulations provide a clearer understanding of how H_{XOY} changes with the vertical angular deviation. The computational model remains consistent with that presented in Section 2.2, employing a uniform half-space with a resistivity of 100 Ω·m. The source is aligned along the X-axis, with its origin at the coordinate center. The polar moment of the source is set at 1 A·m, the receiving angle at 80°, and the transceiver distance at 10 km. Figure 5 illustrates the plotted data for H_{XOY} at 100 Hz (p=28). When the sensor is vertically deflected in the X-axis, the error of H_{XOY} remains relatively stable and approaches zero. Conversely, when the sensor is vertically deflected in the Y-axis, the error of H_{XOY} increases with the increase of the deflection angle, yet remains below 5% for a 20° deflection. This suggests a substantial angular tolerance of H_{XOY}. When the sensor experiences deflection in both the X- and Y-axes, the error of H_{XOY} is determined by the aggregate errors of the two individual directions of deflection.

3.2 Responsiveness analysis results

Assessing the viability of utilizing H_{XOY} and H_{XYZ} for detection requires the calculation of apparent resistivity and an examination of their responsiveness to geological strata. Previous studies predominantly focused on the calculation method for the apparent resistivity of the single-component

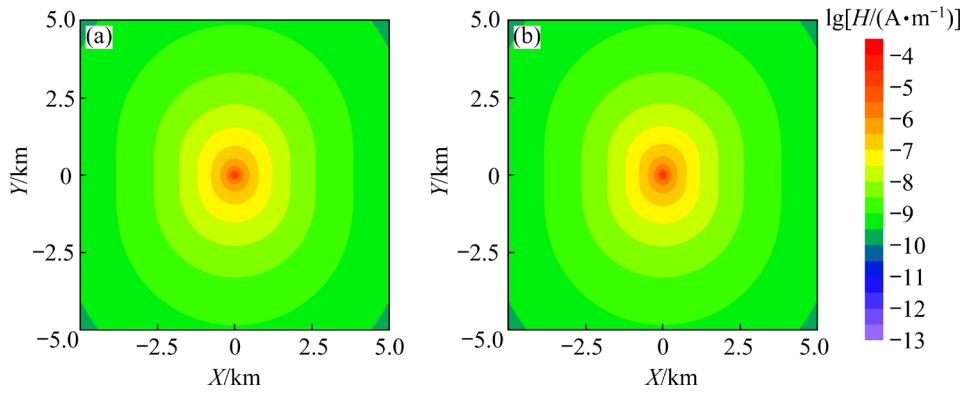

Fig. 4 Radiation patterns of H_{XOY} (a) and H_{XYZ} (b) at 100 Hz

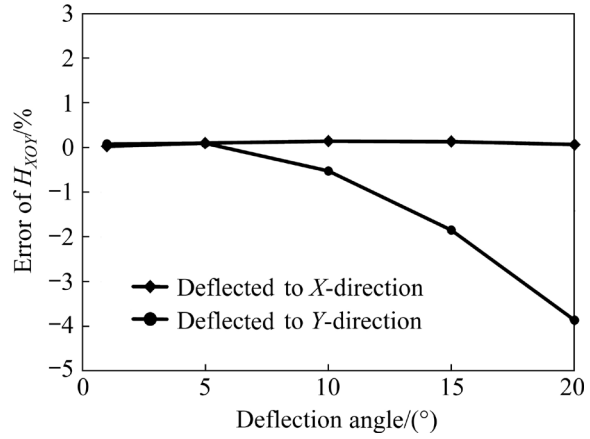

Fig. 5 Error of H_{XOY} affected by angular deviation in vertical direction

magnetic field intensity, with less attention given to those for H_{XOY} and H_{XYZ}. Utilizing the analytical expression for H_{XOY} (Eq. (8)), we can derive an expression for the apparent resistivity of the horizontal magnetic field intensity $\rho_{H_{XOY}}$:

$$\rho_{H_{XOY}}=\frac{\mathrm{i}\omega\mu}{\omega^2\mu\varepsilon-F_{H_{XOY}}} \tag{9}$$

where

$$F_{H_{XOY}}=\left[\frac{\left(\dfrac{16H_{XOY}^2\pi^2r^4}{IdL\sin^2\varphi}-\dfrac{I_1^2K_1^2\cos^2\varphi}{\sin^2\varphi}\right)^{1/2}-6I_1K_1}{\mathrm{i}r(I_1K_0-I_0K_1)}\right]^2 \tag{10}$$

Equation (9) involves a complex expression that includes Bessel functions and device coefficients. It cannot be directly solved for apparent resistivity and requires calculation using iterative methods (or inverse spline interpolation) as detailed by WANG and XIONG [33]. Similarly, an expression for the apparent resistivity of H_{XYZ} can be derived. However, this formula is intricate and currently only solvable using the iterative methods (or inverse spline interpolation). Further details will not be reiterated here.

We evaluate the responsiveness of the apparent resistivity of H_{XOY} and H_{XYZ} to the underground medium by comparing it to that of single-component magnetic field intensity and electric field intensity component along the X-axis (E_X). Homogeneous half-space, H-type, and K-type models, along with HK-type models, have been systematically developed, with their respective parameters listed in Table 1. The source is oriented along the X-axis, centered at the coordinate origin, with a polar moment of 1 A·m, a transceiver angle of 80°, and a transceiver distance of 10 km.

Table 1 Parameters of different forward models

Model	Layered resistivity/(Ω·m)	Layered thickness/m
Homogeneous half-space	100	∞
H-type	100−10−100	100−10−∞
K-type	100−1000−100	100−100−∞
HK-type	100−10−100−10	100−50−100−∞

The results of the forward simulations are presented in Fig. 6. Notably, the apparent resistivities for each single-component magnetic field intensity, as well as for H_{XOY} and H_{XYZ} across all four models, demonstrates significant consistency. Furthermore, when these results are juxtaposed with the apparent resistivity of E_X, they also exhibit a high degree of coherence. This underscores the robust responsiveness of H_{XOY} and H_{XYZ} to the underground medium, substantially fulfilling the requirements for detection.

4 Field experiment results

To validate detection capabilities of the horizontal and total magnetic field strengths, a series of experiments were conducted in the 816 Nuclear Engineering Area in Chongqing, China (Fig. 7) to assess their response to an artificial underground cavern. The cavern connects the exterior through a horizontal passage approximately 400 m in length and 5 m in width. It extends to a maximum depth of about 150 m within the mountain, broadens to approximately 100 m in the main body, and reaches a maximum height of about 80 m. The experiments involved setting up two measurement lines perpendicular to the orientation of the cavern, with a transceiver distance of approximately 2 km and a polar distance of about 500 m. Line 1 has a length of 1590 m (stations 100−1690 m), and Line 2 has a length of 790 m (stations 100−890 m), with the cavern positioned between stations 500−600 m.

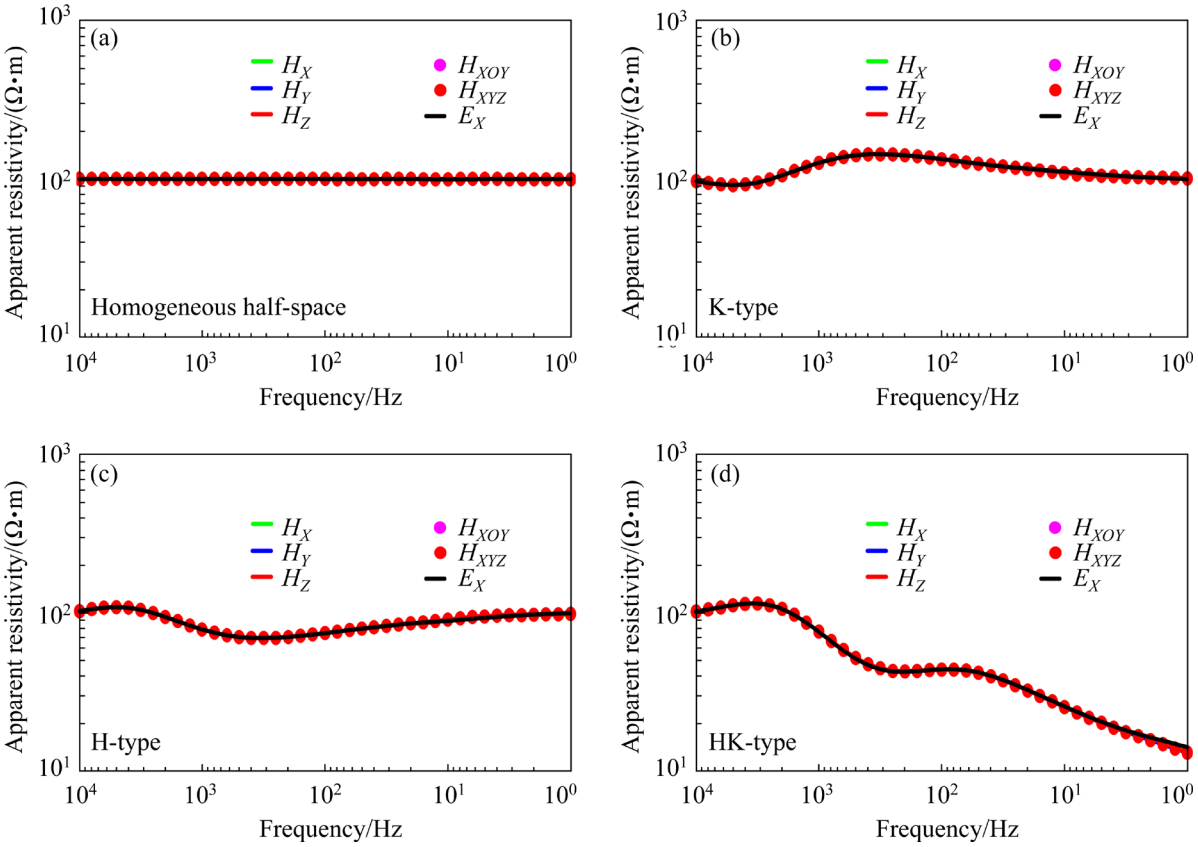

Fig. 6 Apparent resistivities of different magnetic field intensities and E_X

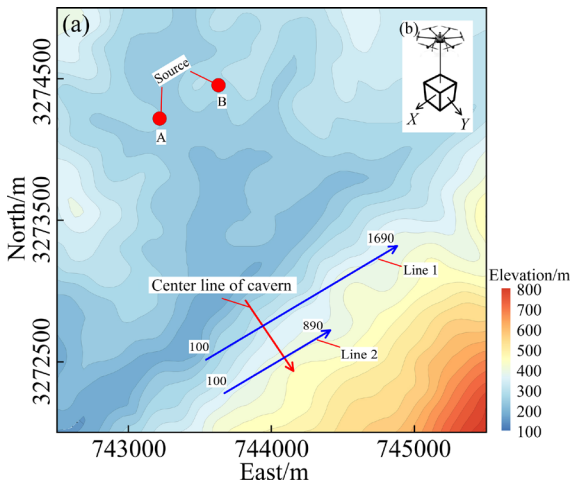

Fig. 7 Distribution of source and survey lines (a), and semi-airborne two-component magnetic field receiver (b)

4.1 Ground-level horizontal and total magnetic field intensities

The ground H_{XOY} was collected using an orthogonal two-component coil at stations spaced every 10 m along Line 2. A current of approximately 60 A was applied, covering a frequency range from 8000 to 125 Hz, with 13 frequencies, logarithmically and uniformly distributed. The coil was precisely leveled horizontally during data acquisition. However, the channels were not strictly aligned with the horizontal components H_X and H_Y, rendering the individual components of the limited practical significance. Consequently, the analysis focused on the synthesized H_{XOY} rather than on individual components. Figure 8(a) reveals significant amplitude anomalies in the ground-level H_{XOY} at the cavern's location, confirming the capability of the horizontal magnetic field strength to detect features of the underground medium. Owing to the current unavailability of three-component magnetic field sensors, it is not possible to directly measure all three orthogonal components of the total magnetic field intensity. In this study, the H_{XYZ} is synthesized by separately collecting the H_{XOY} and H_Z. Since ensuring the accuracy of H_Z measurements from a UAV-mounted sensor is challenging, synthesizing a high-precision H_{XYZ} with H_{XOY}, becomes unfeasible. This study, therefore, conducts experiments by collecting H_Z on the ground and synthesizing the H_{XYZ} with the ground H_{XOY}. Ground measurements

ensure the accuracy of H_{XYZ} and the effectiveness of the experiment.

Due to the significant environmental electromagnetic interference, data of H_{XOY} and H_Z were collected only within the 370−700 m range on Line 2. Consequently, calculations of the H_{XYZ} were confined to this specific section. Figures 8(b) and (c) reveal pronounced magnetic field intensity anomalies in H_Z between 500 and 600 m, with corresponding anomalies in H_{XYZ} at the same location. Figure 9 displays the apparent resistivity and apparent depth results for H_{XOY} and H_{XYZ}. Notably, the apparent resistivity anomalies between 500 and 600 m are prominent in H_{XOY} and H_{XYZ}, aligning closely with the location of the cavern. This underscores the efficacy of H_{XOY} and H_{XYZ} in ground-level detection.

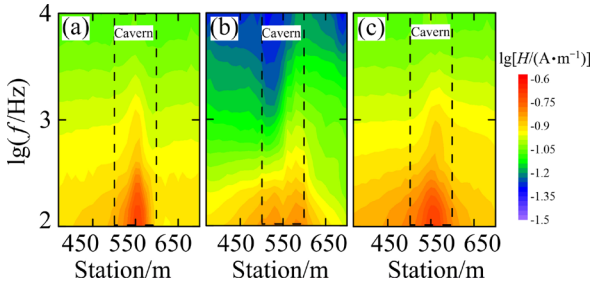

Fig. 8 Cross-sections of ground-level H_{XOY} (a), H_Z (b) and H_{XYZ} (c)

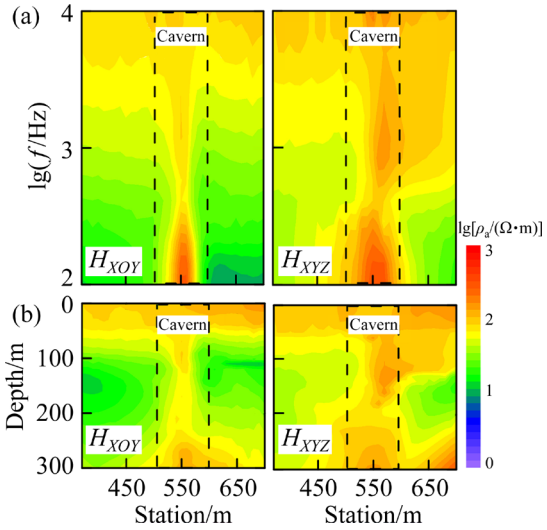

Fig. 9 Apparent resistivity (ρ_a) (a) and apparent depth (b) of ground-level H_{XOY} and H_{XYZ}

4.2 Semi-airborne horizontal magnetic field intensity

The source transmitted a current of about 25 A within a frequency range from 8192 to 24 Hz, comprising 35 frequencies logarithmically and uniformly distributed. Data acquisition employed a two-component magnetic sensor suspended from an UAV. The UAV maintained a speed of 2 m/s at an altitude of approximately 50 m above the ground, with the sensor positioned 15 m below the UAV. Segmentation and calculations were conducted based on a flight time of 5 s and a station distance of 10 m. We adhered to conventional SAEM protocols to gather the H_X and H_Y components of H_{XOY}. Despite the sensors being unable to maintain perfectly accurate angles in the air, which introduced some errors in both components, the data obtained remained high quality.

Figure 10(a) illustrates that the H_X of Line 1 in Fig. 7 exhibits a low-amplitude region between 600 and 1200 m, corresponding to the zero-value band of H_X in the direction perpendicular to the source. This occurs because the zero-value band typically retains a certain degree of magnetic field intensity due to ambient noise. H_Y forms an arc with high magnetic field intensity at the center and lower values on both sides. The H_X and H_Y patterns of Line 2 in Fig. 7 (Fig. 10(b)) mirror the profile of corresponding stations on Line 1. The H_{XOY} for Lines 1 and 2 forms an arc with a higher center and lower sides, similar to H_Y. Both lines exhibit noticeable high-amplitude anomalies between 500 and 600 m, aligning well with the cavern's location. These anomalies are more pronounced in H_X and H_{XOY}. Apparent resistivities for H_X, H_Y, and H_{XOY} are calculated individually, as depicted in Fig. 11. The apparent resistivity of H_X in both lines exhibits high-resistance anomalies between 500 and 600 m, with significant deviations near the zero-value band attributed to environmental noise. H_Y shows a minor anomaly at the cavern location, while H_{XOY} presents a strip-like high-resistance anomaly. Upon combining the apparent depth (Fig. 12) and the apparent resistivity (Fig. 11), it is evident that H_X is influenced by the zero-value band, resulting in pseudo-anomalies, and the anomalous response of H_Y is weak and not intuitive. In contrast, H_{XOY} exhibits no pseudo-anomalies, and its response to the target is both significant and intuitive. This underscores the advantages of H_{XOY} in detection.

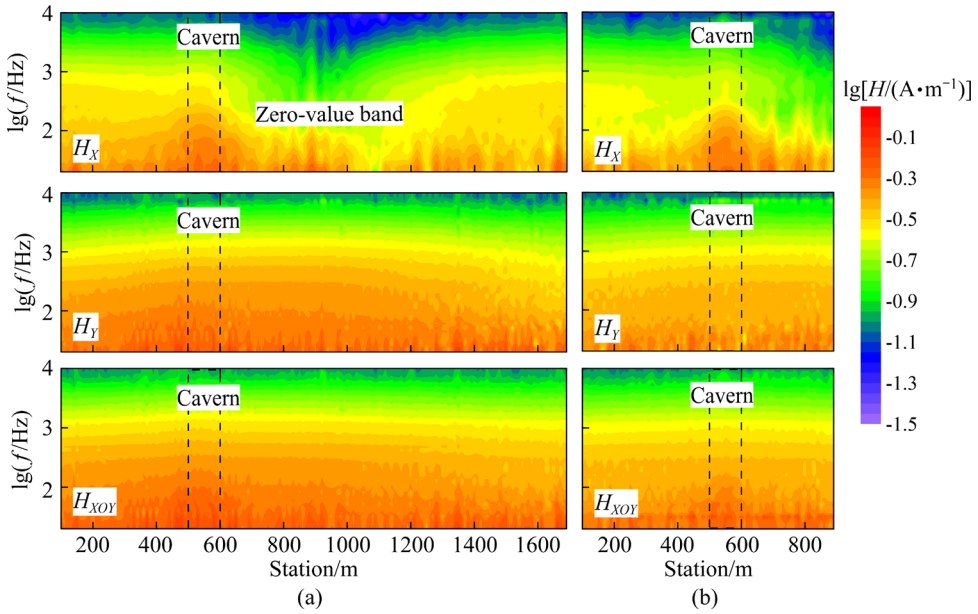

Fig. 10 Semi-airborne magnetic field intensities for Line 1 (a) and Line 2 (b) in Fig. 7

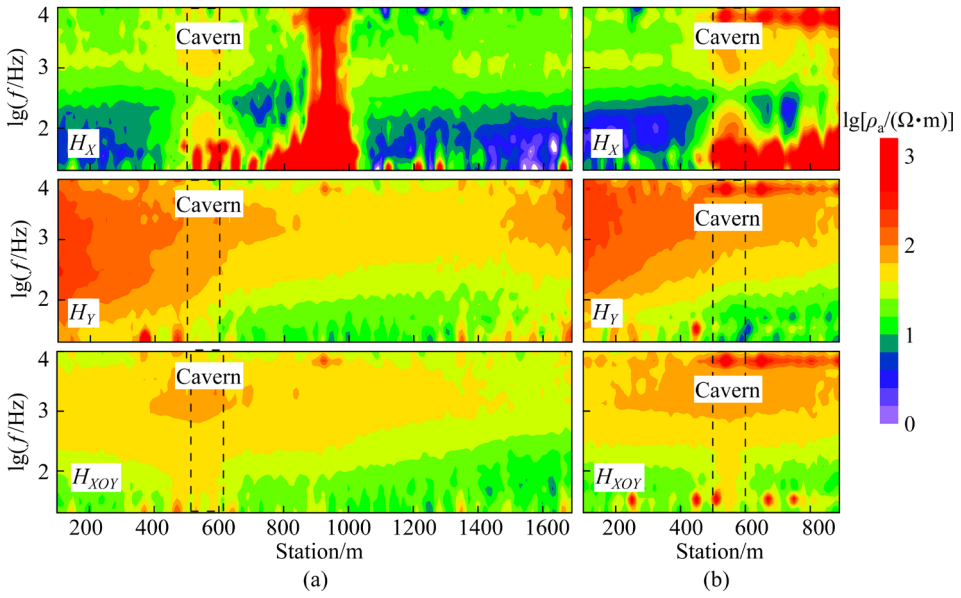

Fig. 11 Apparent resistivities of semi-airborne magnetic field intensities for Line 1 (a) and Line 2 (b) in Fig. 7

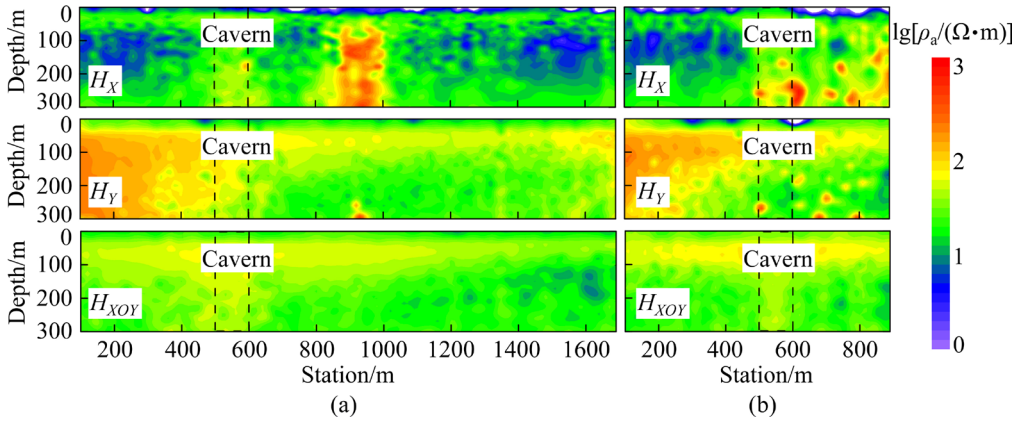

Fig. 12 Apparent depth of semi-airborne magnetic field intensities for Line 1 (a) and Line 2 (b) in Fig. 7

5 Discussion

The concept of "wide azimuth" introduced in this paper encompasses two aspects. First, it considers the orientation of the measurement station in relation to the source. Both H_{XOY} and H_{XYZ} can be observed in any orientation relative to the source, effectively addressing the issue of the zero-value band in single-component magnetic field intensity. This extension enhances the detectable range and improves source utilization. Second, it refers to the angle between the sensor and the source. The H_{XOY} disregards the sensor's angle in the horizontal direction, and the H_{XYZ} completely ignores the sensor's angle, thus resolving the angle error issue of the sensor.

In field experiments, both semi-airborne and ground-level magnetic field intensity detections exhibit a high resistivity response to the underground cavern. However, differences in the responses primarily arise from variations in detection methods and data processing. During actual detection, semi-airborne observations typically employ continuous detection, which introduces more sources of interference. Continuous time-domain data undergoes segmented data processing, resulting in poorer short-term data quality, higher averaging effects for long-term data, lower lateral resolution (associated with flight speed), and weaker responses to anomalies. In contrast, ground-level observations use a single-station detection mode, ensuring higher data quality and more pronounced anomaly responses.

In the experiments, measurements of H_{OXY} show promising results, yet practical applications face significant challenges. One issue is the angular deviation in sensors, which is particularly problematic at low frequencies where the vertical component is comparable to the horizontal component. This can introduce errors, compromising data accuracy. Moreover, while current aircraft is equipped with attitude sensors, which are not integrated with the magnetic field sensors, preventing the correction of angular deviations. These limitations hinder the practical use of H_{XOY}. Additionally, H_{XOY} measurements, although theoretically immune to sensor attitude, still face practical challenges due to the flexible connection between the magnetic field sensor and the aircraft. This flexibility causes the sensor's orientation to fluctuate, leading to potential interference during the movement. To minimize this problem, it is essential to maintain the magnetic field sensor in a stable position and avoid operations in windy conditions that could induce significant angular changes. This approach ensures more reliable and accurate data in field applications.

6 Conclusions

(1) Numerical simulations and experiments have demonstrated the feasibility of frequency-domain CSEM detection of both the horizontal and total magnetic field intensities, and their geoelectric response capability is comparable to that of single-component magnetic field intensity.

(2) The horizontal magnetic field intensity continues to face challenges related to angular deviation in the vertical direction, restricting its wider application.

(3) The total magnetic field intensity effectively eliminates angular errors and zero-value band limitations, thereby enabling wide-azimuth detection at angles of 0°−360° around the field source and offering greater application potential.

CRediT authorship contribution statement

Di-quan LI: Conceptualization, Supervision, Writing – Original draft, Methodology; **Yun-qi ZHU:** Conceptualization, Data curation, Writing – Review & editing, Methodology; **Wei-tian WU** and **Yan-fang HU:** Data curation, Investigation; **Tie-gang TONG:** Resources, Writing – Review & editing.

Declaration of competing interest

The authors declare that they have no known competing financial interests or personal relationships that could have appeared to influence the work reported in this paper.

Acknowledgments

This study was financially supported by the National Key Research and Development Program of China (No. 2022YFC2903704), the Hunan Provincial Science and Technology Innovation Program, China (No. 2023RC1014), the Fundamental Research Funds for the Central Universities of Central South University, China (No. 2023ZZTS0441), and the Hunan Provincial

Natural Science Foundation of China (Nos. 2023JJ40222, 2024AQ2002).

References

[1] DAI Qian-wei, DUAN Dan, LIU Biao, WU Qian-hong, YAN Jia-bin, KONG Hua, CHEN She-fa, ZONG Qi, TANG Yu-yu. Deep exploration of W−Sn and Cu polymetallic deposits in middle Qin−Hang metallogenic belt, South China [J]. Transactions of Nonferrous Metals Society of China, 2023, 33: 231−253.

[2] VOZOFF K. The magnetotelluric method in the exploration of sedimentary basins [J]. Geophysics, 1972, 37: 98−141.

[3] GOLDSTEIN M A, STRANGWAY D W. Audio-frequency magnetotellurics with a grounded electric dipole source [J]. Geophysics, 1975, 40: 669−683.

[4] DI Qing-yun, XUE Guo-qiang, FU Chang-ming, WANG Ruo. An alternative tool to controlled-source audio-frequency magnetotellurics method for prospecting deeply buried ore deposits [J]. Science Bulletin, 2020, 65: 611−615.

[5] DI Qing-yun, XUE Guo-qiang, YIN Chang-chun, LI Xiu. New methods of controlled-source electromagnetic detection in China [J]. Science China Earth Sciences, 2020, 63: 1268−1277.

[6] XUE Guo-qiang, LI Hai, HE Yi-ming, XUE Jun-jie, WU Xin. Development of the inversion method for transient electromagnetic data [J]. IEEE Access, 2020, 8: 146172−146181.

[7] HU Yan-fang, LI Di-quan, YUAN Bo, SUO Guang-yun, LIU Zi-jie. Application of pseudo-random frequency domain electromagnetic method in mining areas with strong interferences [J]. Transactions of Nonferrous Metals Society of China, 2020, 30: 774−788.

[8] SMITH R S, ANNAN A P, MCGOWAN P D. A comparison of data from airborne, semi-airborne, and ground electro-magnetic systems [J]. Geophysics, 2001, 66: 1379−1385.

[9] LIN Jun, KANG Li-li, LIU Chang-sheng, REN Tong-yang, ZHOU Hai-gen, YAO Yao, YU Sheng-bao, LIU Teng, LIU Peng, ZHANG Ming. The frequency-domain airborne electromagnetic method with a grounded electrical source [J]. Geophysics, 2019, 84: E269−E280.

[10] AUKEN E, PELLERIN L, CHRISTENSEN N B, SØRENSEN K. A survey of current trends in near-surface electrical and electromagnetic methods [J]. Geophysics, 2006, 71: G249−G260.

[11] GUO Zhen-wei, LI Fang-da, LIU Jian-xin, YANG Bin, WANG Yan-yi. Research progress of geophysical exploration in marine minerals deposits [J]. The Chinese Journal of Nonferrous Metals, 2023, 33: 285−306. (in Chinese)

[12] LIU Jian-xin, LIU Rong, GUO Rong-wen, TONG Xiao-zhong, XIE Wei. Research progress of electromagnetic method in nonferrous metal mineral exploration [J]. The Chinese Journal of Nonferrous Metals, 2023, 33: 261−284. (in Chinese)

[13] SMIRNOVA M V, BECKEN M, NITTINGER C, YOGESHWAR P, MÖRBE W, ROCHLITZ R, STEUER A, COSTABEL S, SMIRNOV M Y, The desmex Working Group. A novel semiairborne frequency-domain controlled-source electromagnetic system: Three- dimensional inversion of semiairborne data from the flight experiment over an ancient mining area near Schleiz, Germany [J]. Geophysics, 2019, 84: E281−E292.

[14] BECKEN M, NITTINGER C G, SMIRNOVA M, STEUER A, MARTIN T, PETERSEN H, MEYER U, MÖRBE W, YOGESHWAR P, TEZKAN B, MATZANDER U, FRIEDRICHS B, ROCHLITZ R, GÜNTHER T, SCHIFFLER M, STOLZ R, The desmex Working Group. DESMEX: A novel system development for semi-airborne electromagnetic exploration [J]. Geophysics, 2020, 85: E253−E267.

[15] SUN Huai-feng, ZHANG Nuo-ya, LI Dun-ren, LIU Shang-bin, YE Qiong-yao. The first semi-airborne transient electromagnetic survey for tunnel investigation in very complex terrain areas [J]. Tunnelling and Underground Space Technology, 2023, 132: 104893.

[16] NABIGHIAN M N. Electromagnetic methods in applied geophysics (Volume 1, Theory) [M]. Tulsa: Society of Exploration Geophysicists, 1988.

[17] MOGI T, KUSUNOKI K, KAIEDA H, ITO H, JOMORI A, JOMORI N, YUUKI Y. Grounded electrical-source airborne transient electromagnetic (GREATEM) survey of Mount Bandai, north-eastern Japan [J]. Exploration Geophysics, 2009, 40: 1−7.

[18] WANG Yong-fei, GUO Rong-wen, LIU Jian-xin, LI Jian, LIU Rong, CHEN Hang, CAO Xun, YIN Zi-hui, CAO Chuang-hua. A divergence-free vector finite-element method for efficient 3D magnetotelluric forward modeling [J]. Geophysics, 2024, 89: E1−E11.

[19] XUE Guo-qiang, ZHOU Nan-nan, SU Ben-xun, ZHANG Ai-kui, YANG Yan-chen, MO Jiang-ping, WU Xin. Geophysical exploration strategy for Cu−Ni−Co deposits in China: A review [J]. Geophysics, 2024, 89: WB25−WB34.

[20] ZHANG Xin-hao, WANG He, PANG Xiao-yu, YU Sheng-bao. An MFHPWM-based broadband transmitting system for frequency-domain electromagnetic prospecting [J]. IEEE Transactions on Instrumentation and Measurement, 2024, 73: 2001011.

[21] WU Xin, XUE Guo-qiang, FANG Guang-you, LI Xiu, JI Yan-ju. The development and applications of the semi-airborne electromagnetic system in China [J]. IEEE Access, 2019, 7: 104956.

[22] LIU Chang-sheng, LIANG Jie, KANG Ning, LI Zhuo-wei. Sensitive characteristics of contributed region and detectability analysis for semi-airborne frequency-domain electromagnetic system [J]. Journal of Applied Geophysics, 2023, 215: 105116.

[23] ZHANG Ying-ying, LI Xiu, YAO Wei-hua, ZHI Qing-quan, LI Jia. Multi-component full field apparent resistivity definition of multi-source ground-airborne transient electro-magnetic method with galvanic sources [J]. Chinese Journal of Geophysics, 2015, 58: 2745−2758. (in Chinese)

[24] LING Fan. Research on key technologies of ground-airborne wide field electromagnetic receiving system [D]. Changsha: Central South University, 2020. (in Chinese)

[25] LU Jun-tao, WANG Xu-ben, XU Zheng-wei, ZHDANOV M S, GUO Ming, TENG Min-qiang, LIU Zhen. Quasi-2-D robust inversion of semi-airborne transient electromagnetic

data with IP effects [J]. IEEE Transactions on Geoscience and Remote Sensing, 2022, 60: 2008210.

[26] JI Yan-ju, WANG Shi-peng, YU Yi-bing, LUAN Hui, WANG Yuan, GAO Quan-ming, ZHAO Xue-jiao. 3-D modeling and analysis of small-loop source TDEM method based on CFS-PML-CN-FDTD method [J]. IEEE Transactions on Geoscience and Remote Sensing, 2024, 62: 2001214.

[27] YANG Yang, HE Ji-shan, LI Di-quan. Energy distribution and effective components analysis of 2^n sequence pseudo-random signal [J]. Transactions of Nonferrous Metals Society of China, 2021, 31: 2102−2115.

[28] CHEN Tao, YANG Di-kun. Modeling and inversion of airborne and semi-airborne transient electromagnetic data with inexact transmitter and receiver geometries [J]. Remote Sensing, 2022, 14: 915.

[29] LIU Zheng-guang, REN Zheng-yong, YAO Hong-bo, TANG Jing-tian, LU Xu-shan, FARQUHARSON C. A parallel adaptive finite-element approach for 3-D realistic controlled-source electromagnetic problems using hierarchical tetrahedral grids [J]. Geophysical Journal International, 2023, 232: 1866−1885.

[30] HE Ji-shan. Wide field electromagnetic sounding methods and pseudo-random signal coding electrical method [M]. Beijing: Higher Education Press, 2010. (in Chinese)

[31] WANG Zhen-xing. One-dimensional forward and inversion for wide field electromagnetic method basic on single electromagnetic component [D]. Changsha: Central South University, 2020. (in Chinese)

[32] QIU Shi-lin, MA Bin-yuan, WU Qiong, QU Run-zu, SHI Bo-ri, LUAN Hui, JI Yan-ju. Numerical calculation of diffusion depth and skin depth based on a GEMTIP model in electromagnetic sounding methods [J]. IEEE Transactions on Geoscience and Remote Sensing, 2022, 60: 4512209.

[33] WANG Shun-guo, XIONG Bin. Numerical calculation methods of wide field apparent resistivity [J]. Computing Techniques for Geophysical and Geochemical Exploration, 2012, 34: 380−384. (in Chinese)

基于水平磁场和总磁场强度的宽方位 CSEM 探测

李帝铨[1,2,3]，朱云起[1,2,3]，伍炜天[1,2,3]，胡艳芳[1,2,3]，佟铁钢[1,2,3]

1. 有色金属成矿预测与地质环境监测教育部重点实验室(中南大学)，长沙 410083；
2. 有色资源与地质灾害探测湖南省重点实验室，长沙 410083；
3. 中南大学 地球科学与信息物理学院，长沙 410083

摘　要：传统人工源电磁法一般采集总磁场强度的单个分量，导致出现零值带、探测方位角小和角度偏差等缺陷。本文作者提出了利用水平磁场强度和总磁场强度进行探测的方法。通过数值模拟分析了传感器角度偏差对单分量和水平磁场强度的影响程度。水平磁场强度不受传感器水平角度偏差影响，而总磁场强度则完全不受角度限制，理论上利用正交磁传感器可以实现宽方位磁场探测。现场试验结果显示，水平磁场强度和总磁场强度对地下空洞均有明显的异常响应，这些试验证明磁传感器角度偏差相关问题得到了显著减少，验证了利用水平磁场强度和总磁场强度进行探测的可行性。本文提出的宽方位探测方法将人工源电磁法的可探测方位角扩展到 360°，解决了磁场传感器的角度偏差问题，从而提高了探测精度。

关键词：人工源电磁法；宽方位；磁场；零值带；角度偏差

(Edited by Wei-ping CHEN)